Selective oxidation of aluminium in Mo(Al,Si)$_2$

Ding, Zhaoying; Brouwer, Johannes C.; Kwakernaak, Cees; Hermans, Marcel J.M.; Popovich, Vera; Quadakkers, Willem J.; Sloof, Willem G.

Important note
To cite this publication, please use the final published version (if applicable).
Please check the document version above.

Selective oxidation of aluminium in Mo(Al,Si)$_2$

Zhaoying Ding [a], Johannes C. Brouwer [a], Cees Kwakernaak [a], Marcel J.M. Hermans [a],
Vera Popovich [a], Willem J. Quadakkers [b], Willem G. Sloof [a,*]

[a] Department of Materials Science and Engineering, Delft University of Technology, Mekelweg 2, 2628 CD Delft, the Netherlands
[b] Forschungszentrum Jülich GmbH, IEK-2, Jülich 52428, Germany

ARTICLE INFO

ABSTRACT

Mo(Al$_x$Si$_{1-x}$)$_2$ alloy with x in the range of 0.35–0.65 were prepared by a one-step spark plasma sintering. To study the exclusive formation of an α-Al$_2$O$_3$ scale, oxidation experiments were conducted in low and high oxygen partial pressure ambient at 1373 K; viz.: 10^{-14} and 0.21 atm. The oxidation kinetics follows a parabolic rate law after a transient period. A counter-diffusion process of O and Al along grain boundaries of Al$_2$O$_3$ scale is responsible for the equiaxed and columnar grain growth based on a two-layered microstructure. The formation of a dense equiaxed α-Al$_2$O$_3$ layer contributes to excellent oxidation resistance.

1. Introduction

Molybdenum disilicide (MoSi$_2$), is an attractive material for structural high-temperature applications due to its high melting point (above 2273 K) in combination with a moderate density (6.24 g/cm^3) and an excellent oxidation resistance in the temperature up to approximately 2000 K [1–4]. Currently, potential applications of MoSi$_2$ include furnace elements and components for high-temperature heat exchangers and filters, gas burners, components for hot-section jet engines and gas turbines [5,6]. However, a high creep rate at elevated temperatures [1, 2] and the so-called 'pesting' phenomena whereby disintegration occurs during oxidation at temperatures in the range of 650–800 K [1–3] have inhibited practical application of this compound, but initiated an intensified research in MoSi$_2$-based alloys [1,2,4–7].

High-temperature oxidation resistance can be realized with suitable alloying elements, typically Al, Si and Cr [8], whose preferential oxidation can create a diffusion barrier to oxygen permeation [9–11]. The effect of third elements in Mo-Si-X (with X as Al, Ta, Ti, Zr and Y) intermetallics on the high-temperature oxidation [12,13] and pesting behaviour [14,15] has been investigated. Among these alloys, the Mo-Si-Al intermetallic has proven to be the most promising [1,6,15].

Partial substitution of Si with Al improves the oxidation resistance of MoSi$_2$ due to the formation of a protective alumina scale via an in-situ displacement reaction [11,16,17]. The alumina scale formed from Mo (Al,Si)$_2$ is stable and adherent with a close match of thermal expansion coefficient between the bulk material and Al$_2$O$_3$ [8,18], viz.: 7.4–8.6 ×

10^{-6} K^{-1} [19] and 8.1–8.9 × 10^{-6} K^{-1} [20], respectively. This is a major advantage compared to silica forming MoSi$_2$, which exhibits evaporation in reducing environments and spalling of the oxide scale [11,12,17, 18].

Several studies have been carried out to assess the properties of Mo (Al,Si)$_2$ materials including their mechanical behaviour [4], thermo-physical properties [21] and oxidation behaviour [1,6,11,13,15, 17,22]. However, the oxidation mechanism remains yet unclear and most of these studies concerns Mo(Al,Si)$_2$ compounds with a relatively low Al substitution. This work, however, focusses on the selective oxidation behaviour of Al in Mo(Si,Al)$_2$ with relatively high Al contents up to about 43 at.%.

2. Materials and methods

2.1. Materials design and sample preparation

To obtain single phase Mo(Al,Si)$_2$ with different high Al content, six batches of elemental powder mixtures were prepared; see Table 1. The target compositions of Mo(Al$_x$Si$_{1-x}$)$_2$ were x equal to 0.40, 0.45, 0.50, 0.55, 0.60 and 0.65; respectively. Elemental powder of molybdenum (2–5 μm, 99.95+ % purity, Chempur, Germany), silicon (45 μm 99.99% purity, TLS Technik GmbH & Co, Germany) and aluminium (45 μm 99.8% purity, TLS Technik GmbH & Co, Germany) were mixed in the desired molar ratios for 3 hours with a Turbula mixer (Willy A. Bachofen AG Maschinenfabrik, Type T2C, Switzerland) using ZrO$_2$ balls with a

Table 1
Chemical composition, constituting phases fractions and lattice parameters of $Mo(Al_xSi_{1-x})_2$ samples prepared by spark plasma sintering.

Nominal x (-)	Actual x (-)	Al fraction* (at.%)	Phase (wt%)	Crystal lattice** (-)	Lattice parameter				
					a (pm)	b (pm)	c (pm)	c/a (-)	b/a (-)
0.40	0.35	23.5 ± 0.5	H: 100.0	C40	472.15(1)	–	657.65(2)	1.393	–
0.45	0.40	26.4 ± 0.4	H: 100.0	C40	472.06(1)	–	657.57(3)	1.393	–
0.50	0.48	31.9 ± 0.1	H: 92.8	C40	474.198(4)	–	660.08(1)	1.392	–
			O: 7.2	C54	826.5(3)	481.2(2)	877.5(3)	1.062	0.582
0.55	0.52	34.9 ± 3.6	H: 85.4	C40	474.78(2)	–	660.90(4)	1.392	–
			O: 14.6	C54	827.0(1)	480.1(1)	879.1(2)	1.063	0.581
0.60	0.58	38.9 ± 0.3	H: 5.7	C40	474.47(3)	–	660.32(7)	1.392	–
			O: 90.2	C54	826.25(2)	479.93(2)	877.77(3)	1.062	0.581
			T: 4.1						
0.65	0.65	43.1 ± 0.5	O: 92.7	C54	826.86(2)	481.88(3)	879.19(4)	1.063	0.583
			T: 7.3						

H: hexagonal $Mo(Al,Si)_2$; O: orthorhombic $Mo(Al,Si)_2$; T: tetragonal $Mo_5(Al,Si)_3$
*As determined with EPMA, cf. Section 2.3.
**In terms of $Mo(Al,Si)_2$

diameter of 5 mm. Next, the powder mixtures were densified and sintered in a spark plasma sintering (SPS) furnace (FCT SPS system, type KCE-FCT HP D-25-SI, Germany). To this end, 6.5 g of the powder mixture was loaded into a graphite die with an inner diameter of 20 mm (ISO-68, Toyo Tanso, Japan). Graphite foils (Permafoil, PF20-HP, Toyo Tanso, Thailand) was used to prevent possible reaction between the powder and the graphite die and punches. Thin layers of BN (Henze, Lauben, Germany) were sprayed onto both sides of the graphite foils for easy removal of the composite sample from the die and punches after sintering. The punches and die assembly with the elemental powder mixture was mounted into the SPS furnace. Then, this furnace was evacuated and flushed two times with Ar-gas of 5N purity (Linde, The Netherlands). Next, the furnace was heated up to 1773 K with a heating rate of 20 K/min. The electric current was applied following 15/5 on/off 3 ms pulse sequence. First, a pressure of 50 MPa was applied till the temperature reached 873 K. Next, the pressure was released to avoid leakage of melted Al. When the temperature reached to 1773 K, a pressure of 50 MPa was applied again to promote alloying and densification. The sample was kept for 30 minutes at the sintering temperature and thereafter cooled naturally to room temperature. The sintered tablet with a diameter of 20 mm and a thickness of about 3 mm was ground with SiC emery paper starting with 80 mesh grit size to finally 1500 mesh grit size to obtain a smooth surface finish. Hereafter, the disc was thoroughly cleaned ultrasonically with isopropanol.

Finally, the sintered discs were cut into rectangular bars of 15 × 8 × 2 mm via electric discharge machining (EDM) for thermogravimetric analysis. The surfaces of these bars were ground with SiC emery paper starting with 800 mesh grit size to finally 4000 mesh grit size. Next, these surfaces were polished subsequently with 3 and 1 μm grains diamond paste on soft cloths. The samples were cleaned ultrasonically in isopropanol and dried by blowing with pure nitrogen (purity better than 5N) before storing into airtight membrane boxes (Agar Scientific G3319, UK).

2.2. Isothermal oxidation

The isothermal oxidation of bulk $Mo(Al_xSi_{1-x})_2$ material was performed in a low oxygen partial pressure (pO_2) of 10^{-14} atm. gas environment at 1373 K to promote the selective oxidation of Al and to avoid possible formation of volatile Mo-oxide species.

The low oxygen partial pressure of 10^{-14} atm. at 1373 K in the gas ambient was realized with a gas mixture of Ar with 8 vol.% CO_2 and 50 vol.% CO; see Appendix A. The oxidation kinetics was monitored with thermogravimetric analysis (TGA) using a dual furnace balance (Setaram TAG 16/18, Caluire, France), which allows automatic correction for buoyancy effects. The alumina furnace tubes have an inner diameter of 15 mm. This analyser is equipped with Pt/Pt-10%Rh (S-

type) thermocouples. The gas mixture was admitted to the TGA analyser via mass flow controllers (Bronkhorst, The Netherlands) operated with Labview (version 2020) such that the total gas flow matches 100 sccm, which was equally divided over both furnace tubes. The gases Ar, CO and CO_2 were supplied from Linde Gas Benelux BV with a purity better than 5N. Prior to admitting the gas mixtures to the furnaces, Ar was filtered to remove any residual moisture and hydrocarbons, with SGT click on oxygen trap (< 5 ppb O_2, SGT Middelburg, The Netherlands), Hydrosorb (< 20 ppb H_2O) and Accosorb (< 10 ppb hydrocarbons) filters (Messer Griesheim, Germany); respectively.

The sample was mounted onto a sapphire rod with an alumina pin having a diameter of 2.2 mm through a hole of diameter of 2.5 mm in the sample. The initial mass of the sample was weighed using a Mettler Toledo balance (accuracy ± 1 μg). A dummy sample of alumina with the same dimensions was mounted onto a sapphire rod of the counter part of the balance to eliminate any buoyancy effect. To flush the gas lines, balance and furnaces, the TGA system was pumped to vacuum (< 50 Pa) and refilled with Ar three times. Then, the dual furnaces were heated up from room temperature to the target temperature with 10 K/min, while purging with 100 sccm Ar, i.e., 50 sccm gas in each furnace. When the target temperature for isothermal oxidation was reached, the gas composition was switched to the oxidation atmosphere while maintaining a total gas flow of 100 sccm for 16 hours. After oxidation, the furnace was cooled down to room temperature with 10 K/min while flushing with pure Ar. The short-term oxidation experiments of 1 hour holding time were conducted using the same condition.

The oxidation behaviour of $Mo(Al_xSi_{1-x})_2$ material at 1373 K was also investigated by direct exposure to a dry synthetic air environment and after pre-oxidation under low oxygen partial pressure condition. Also, in these cases the oxidation kinetics was monitored with thermogravimetric analysis using a dual furnace balance. After 16 hours pre-oxidation under low oxygen partial pressure of 10^{-14} atm. at 1373 K, the gas was switched directly to Ar with 21 vol.% O_2 for another 50 hours. Afterwards, the furnace was cooled to room temperature flushing with pure Ar.

2.3. Characterization

The phase composition of the alloy samples before and after oxidation were determined with X-ray diffractometry (XRD) using a D8 advance diffractometer (Bruker, Germany) in the Bragg-Brentano geometry operated with Cu-Kα radiation. Diffractograms were recorded in the 2θ range of 10–130° with a step size of 0.030° and a counting time of 2 s per step. XRD measurements in the grazing incidence geometry were performed with the same diffractometer with Co-Kα radiation in the 2θ region between 10° and 110° with a fixed observation angle of 3°. The incident beam had a height of 5 mm and a width of 1 mm. A step size of
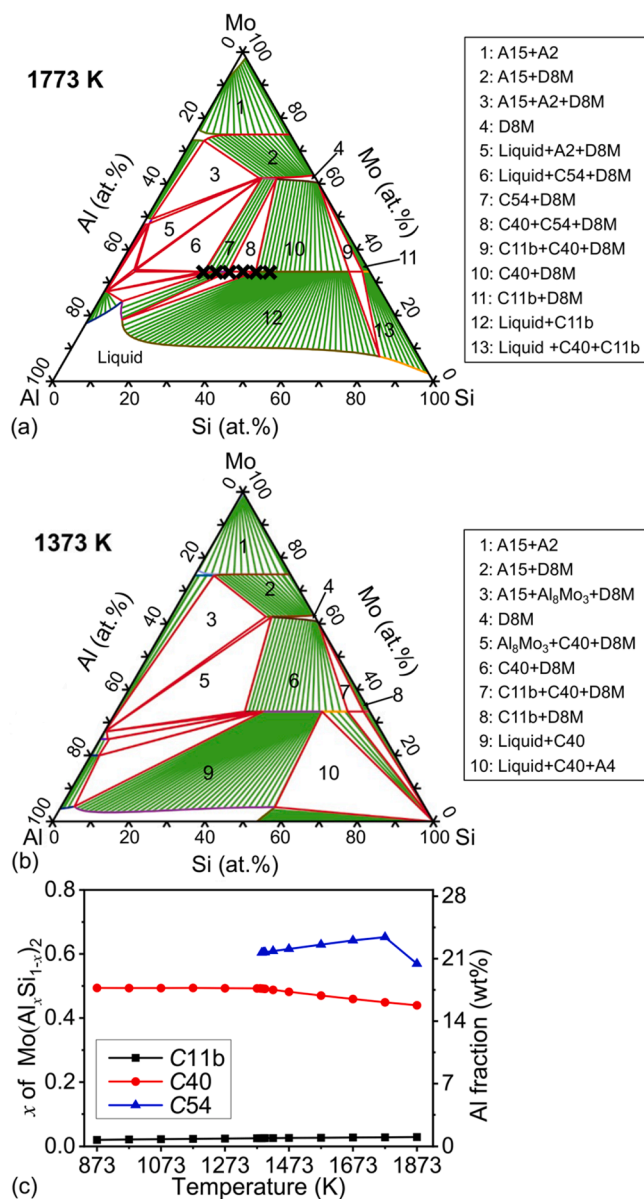
Fig. 1. (a) Mo–Al–Si ternary phase diagram at 1773 K calculated by Thermo-Calc software. The black crosses denote the compositions of the alloys prepared in the present work; (b) Mo–Al–Si ternary phase diagram at 1373 K calculated by Thermo-Calc software; (c) the maximum amount of Al dissolved in Mo(Al$_x$Si$_{1-x}$)$_2$ as a function of temperature. The C11b, C40 and C54 are Mo(Al,Si)$_2$ in tetragonal, hexagonal and orthorhombic crystal lattice, respectively; D8M is Mo$_5$(Al,Si)$_3$ with tetragonal crystal lattice; A15 is Mo$_3$(Al,Si), A2 is AlMo, and A4 is Si with diamond structure.

0.030° 2θ and a counting time of 5 s per step were applied to identify the oxide phases present at the sample surface. These diffractograms were evaluated using the Bruker Diffrac EVA software (version 3.1). Quantitative phase composition analysis and lattice parameters determination were performed with Rietveld refinement [23] using MAUD software (version 2.93).

The surface morphology of the samples was observed with scanning electron microscopy (SEM) using a JEOL JSM 6500 F (JEOL, Japan). This instrument is equipped with an ultra-dry energy dispersive spectrometer (EDS) for X-ray micro analysis (XMA, System 7, Noran, USA). Cross-sections of the samples were prepared and analysed with a dual beam scanning electron microscope (Helios G4 PFIB UXe, Thermo Fisher Scientific, USA) equipped with a xenon plasma focused ion beam (PFIB).
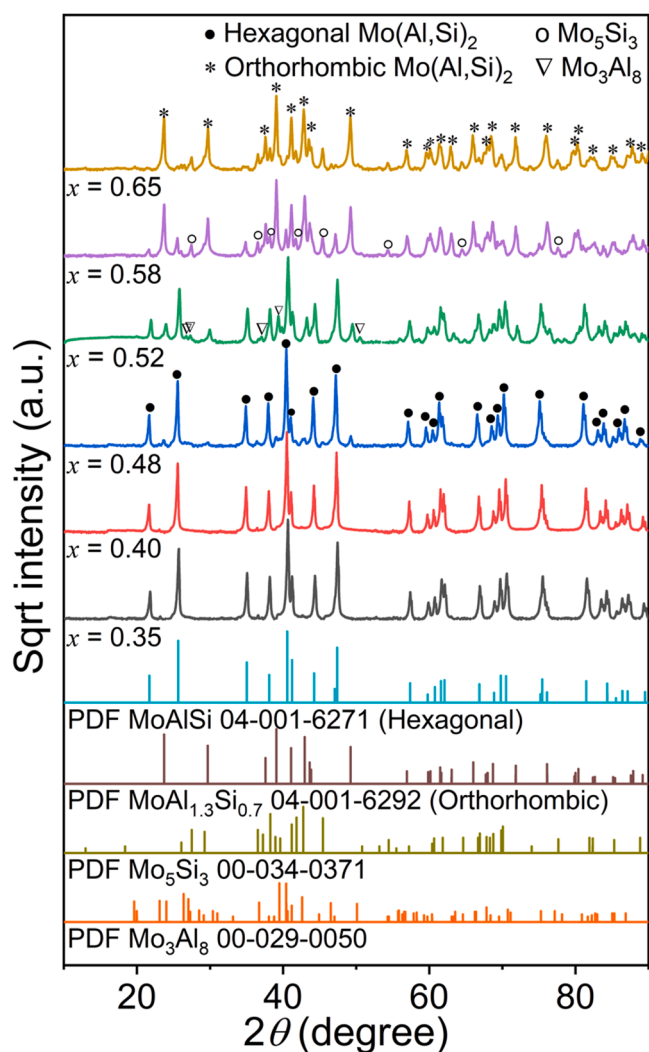
Fig. 2. XRD patterns of Mo(Al$_x$Si$_{1-x}$)$_2$ bulk alloys fabricated by spark plasma sintering.

This instrument is provided with an EDAX system (USA) for energy dispersive X-ray micro analysis with Octane Elite plus detector, using TEAM acquisition and analysis software (version 4.5). First, the surface of the sample was covered with about 2 μm layer of Pt added with C. Next, a trench was cut with the Xe PFIB operated at 30 keV. Then, the surface of the cross-section was polished with a low current Xe PFIB. SEM images and X-ray spectra were recorded using a 10 keV focused electron beam. The thickness of the oxide layer was measured at the cross-section exposed by PFIB milling.

The concentration of Mo, Si, Al and O was determined with electron probe X-ray microanalysis (EPMA). The analysis was performed with a JXA 8900 R (JEOL, Japan) microprobe employing Wavelength Dispersive Spectrometry (WDS). A focussed electron beam was used with an energy of 10 keV and a current of 50 nA. The composition at each analysis location of the sample was determined using the X-ray intensities of the constituting elements after background correction relative to the corresponding intensities of reference materials. In this case, the X-ray intensities of Mo-Lα, Si-Kα, Al-Kα and O-Kα were measured and pure Mo, Si, Al and SiO$_2$, respectively, were used as references. The thus obtained intensity ratios were processed with a matrix correction program CITZAF [24]. The concentration of each element was obtained from the average of at least 80 measurement points.
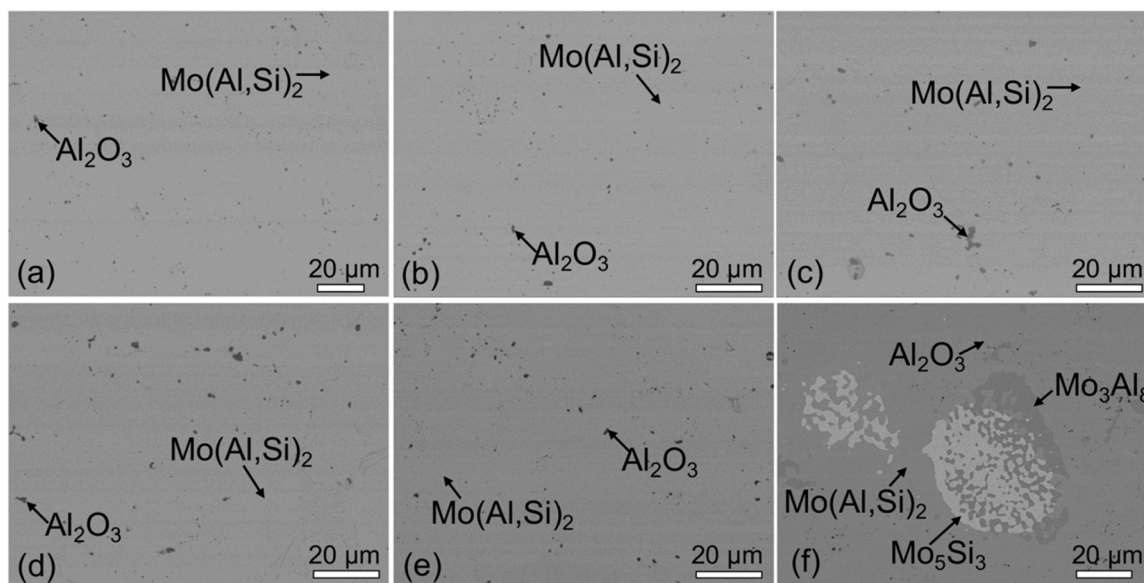
Fig. 3. Microstructures of Mo(Al_xSi_{1-x})$_2$ bulk alloys fabricated by spark plasma sintering of elemental powder mixtures with composition of (a) $x = 0.35$; (b) $x = 0.40$; (c) $x = 0.48$; (d) $x = 0.52$; (e) $x = 0.58$; (f) $x = 0.65$.

3. Results and discussion

3.1. Composition and microstructure of sintered Mo–Si–Al alloys

The Mo–Al–Si ternary phase diagram at different temperatures was constructed with Thermo-Calc software (version 2022a, Thermo-Calc, Stockholm, Sweden) using the thermodynamic database of Al–Si–Mo / Al–Mo–Si–U [25] to investigate the amount of Al that can be dissolved in Mo(Al,Si)$_2$. Fig. 1 shows as examples, the section of the Mo–Al–Si ternary phase diagram at 1773 K and 1373 K as well as the calculated

maximum amount of Al dissolved in Mo(Al_xSi_{1-x})$_2$ as a function of temperature.

Mo(Al,Si)$_2$ appears with three different crystal lattice structures depending on the Al to Si ratio, which include: the tetragonal (*C*11b) structure, the hexagonal (*C*40) structure and the orthorhombic (*C*54) structure. MoSi$_2$ exhibits the tetragonal (*C*11b) structure, which has a small solubility of Al (1.9 at.% at 1773 K). Further substitution of Si with Al results in Mo(Al,Si)$_2$ with hexagonal (*C*40) crystal lattice structure which exists over a wide composition range up to about 30 at.% Al at 1773 K. Beyond this composition, Mo(Al,Si)$_2$ takes the orthorhombic
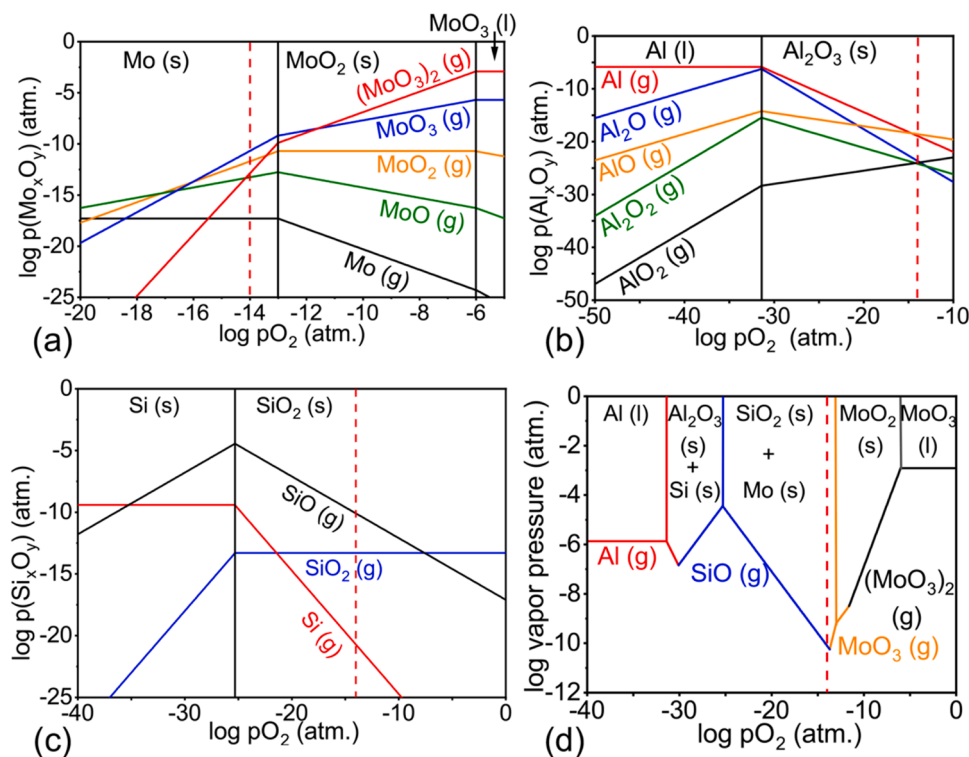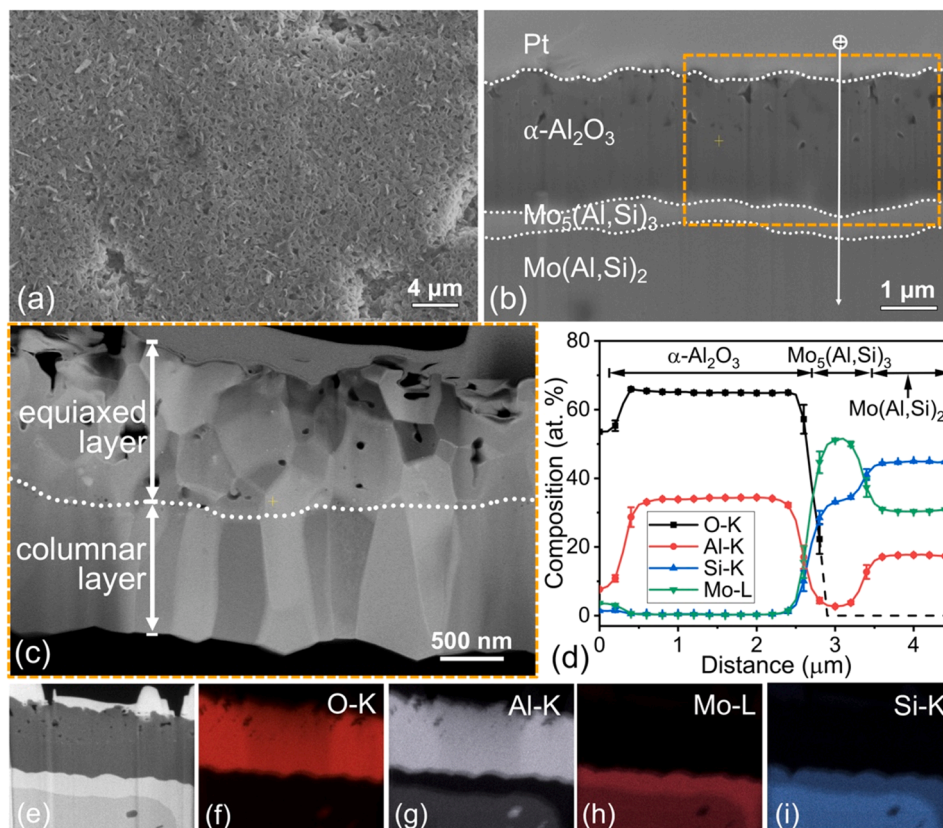

Fig. 4. Stability diagrams at 1373 K for: (a) Mo–O; (b) Al–O; (c) Si–O; and (d) combined diagram presenting the species with the highest vapour pressure as a function of *p*O$_2$. Vertical dashed red line indicates an oxygen partial pressure of 10^{-14} atm..

Fig. 5. SEM surface and cross-section observation of the $Mo(Al_{0.40}Si_{0.60})_2$ after oxidation in low pO_2 (10^{-14} atm.) gaseous ambient at 1373 K for 16 hours: (a) surface morphology; (b) cross-section with position of the composition line scan across the oxide scale, $Mo_5(Al,Si)_3$ layer and $Mo(Al,Si)_2$ substrate; (c) cross-section (STEM image); (d) composition depth profile; (f)-(i) X-ray maps of region (e).

($C54$) crystal lattice structure. As can be seen in Fig. 1c, the largest amount of Al that can be dissolved in $Mo(Al,Si)_2$ at a temperature of about 1773 K occurs when the material features the orthorhombic ($C54$) crystal lattice.

The actual compositions of the fabricated alloy bulk samples determined by EPMA analysis are listed in Table 1. The Al content of the alloys is slightly lower but still very close to the nominal value. The loss of the small amount of Al results from the formation of alumina inclusions.

XRD patterns of the alloys reveal that with increasing amount of Al substituting Si, denoted as x in $Mo(Al_xSi_{1-x})_2$, the crystal lattice changes from a hexagonal type $C40$ to a orthorhombic type $C54$; see Fig. 2. The phase fractions and lattice parameters as determined by the Rietveld refinement are listed in Table 1. These results show that a small fraction of the orthorhombic phase (7.2 %) starts to appear when the Al content is 31.9 at.% in $Mo(Al_xSi_{1-x})_2$ and becomes the dominant phase when the Al content is further increased up to 38.9 at.%. This phase change as a function of the composition is in agreement with the ternary phase diagram of Mo–Al–Si at 1773 K (cf. Fig. 1a) suggesting that the phases are in thermodynamic equilibrium after sintering and stay stable upon cooling to room temperature. $Mo(Al,Si)_2$ is the main phase in the alloy samples. XRD lines of Mo_5Si_3 and small peaks Mo_3Al_8 were also detected for samples with high Al content; see Fig. 2. The Mo_5Si_3 phase can be present already at the synthesis temperature, whereas the Mo_3Al_8 can only be formed during cooling; see the Mo–Al–Si ternary phase at 1773 K in Fig. 1a and at 1373 K in Fig. 1b.

It may be expected that with increasing substitution of Si by Al in $Mo(Al,Si)_2$ the lattice parameters change due to the larger atomic radius of Al atoms (143 pm) compared to Si (117 pm) [21]. However, the variations of lattice parameters for the composition range considered here (i. e., x from 0.35 to 0.65) are very small with increasing amount of Al; see

Table 1. This is in agreement with the work of Tabaru et al. [21], who provided a detailed explanation. The crystal lattice structure of $Mo(Al_xSi_{1-x})_2$ is hexagonal ($C40$) from x is 0.35 till 0.40 when the maximum solubility of Al in this crystal lattice is reached. When the Al content is further increased, the crystal lattice changes from hexagonal ($C40$) to orthorhombic ($C54$).

The alloys fabricated by sintering of elemental powder mixtures exhibit uniform microstructures albeit some patches of alumina were observed, except in the alloy with 43.1 at.% Al ($x = 0.65$); see Fig. 3. Local composition analysis with XMA revealed regions where three phases coexist; see Fig. 3f. These regions comprise $Mo_5(Al,Si)_3$, Mo_3Al_8 and $Mo(Si,Al)_2$, which is formed upon cooling (cf. phase diagram in Fig. 1b) and is consistent with the XRD results (see above).

3.2. Low oxygen partial pressure oxidation of Mo–Si–Al alloys

Isothermal oxidation of bulk $Mo(Al_xSi_{1-x})_2$ material was performed in a low oxygen partial pressure (pO_2) of 10^{-14} atm. gaseous ambient at 1373 K, which is slightly lower than the dissociation pressure of Mo-oxides, but far above the dissociation pressure of Si- and Al-oxides according to the metal/oxide stability diagrams; see Fig. 4a-d. SiO(g) possesses the highest vapour pressure of about 10^{-10} atm. at the target pO_2 of 10^{-14} atm.; see Fig. 4d. The vapour pressure magnitudes will slightly differ for the $Mo(Al,Si)_2$ material since unit activities are assumed for the calculation of this kind of diagram [26–28]. However, when considering ideal thermodynamic behaviour of the $Mo(Al_xSi_{1-x})_2$ alloys, the activity has no influence on the slope of the lines in the oxide stability diagram (Fig. 4) but only make a very small difference on the intercept.

During the oxidation process in such a low pO_2 ambient condition, the solid oxide MoO_2 cannot be formed and the vapour pressures of the

Table 2

Parabolic growth rate constant (k_p) of the oxidation, thicknesses and lateral grain size of the oxide scale.

Isothermal oxidation	pO_2 (atm.)	Gas flow (sccm)*	Al_2O_3 thickness (μm)	k_p (g^{2}m^{-4}h^{-1})	$h_{columnar}/h_{total}$** (-)	Lateral grain size (μm)
16 h low pO_2	10^{-14}	100	2.27 ± 0.11	0.66	0.48	0.31 ± 0.10
16 h low pO_2 then 50 h dry syn. air	10^{-14} 0.21	80	4.19 ± 0.14	0.45 0.70	0.37	0.49 ± 0.14
50 h in syn. air	0.21	80	2.30 ± 0.33	0.25	0.34	0.33 ± 0.07

*A total gas flow of 80 sccm was applied for the oxidation experiment with dry synthetic air.

**Thickness ratio of columnar layer to the total oxide scale.
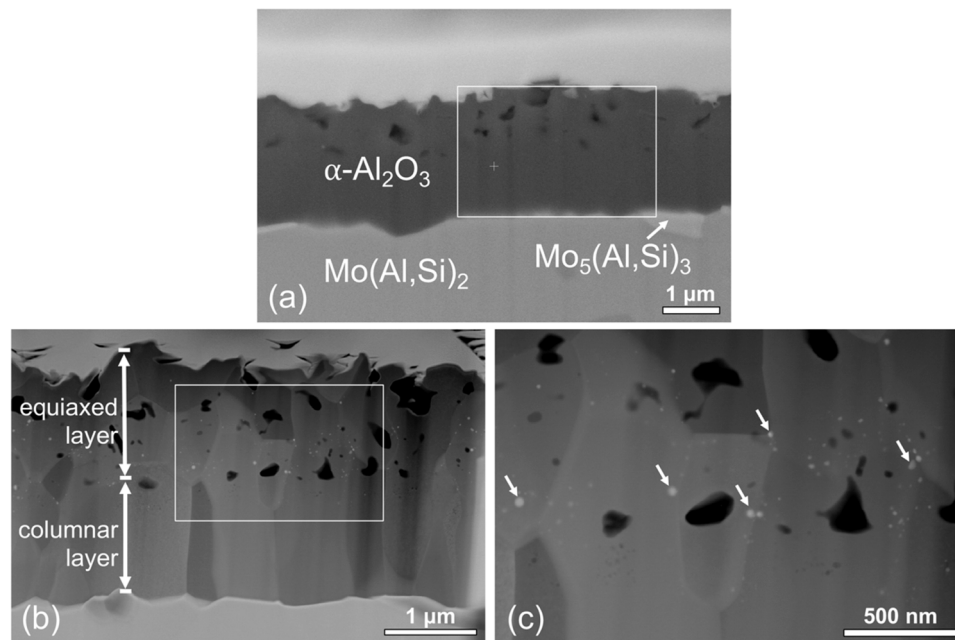
Fig. 6. SEM cross-section observation of the Mo(Al$_{0.65}$Si$_{0.35}$)$_2$ after oxidation in low pO_2 (10^{-14} atm.) gaseous ambient at 1373 K for 16 hours: (a) cross-section (BSE image); (b) cross-section (STEM image) of the area indicated with the white frame in (a); (c) details (STEM image) of the area indicated with the white frame in (b). White arrows in (c) indicate particles of Mo$_5$(Al,Si)$_3$.

volatile Mo-oxides are very low (less than 10^{-10} atm.), according to the oxide stability diagram; cf. Fig. 4. Once the surface of the alloy is covered with a closed layer of either solid silica or alumina, volatile Mo-oxides will likely cease to form. Since the dissociation pressure of Al$_2$O$_3$ is much lower than that of SiO$_2$ (10^{-31} versus 10^{-25} atm., respectively, see Figs. 4b and 4c), alumina will be formed preferentially [29,30].

3.2.1. Oxide scale composition and microstructure

After oxidation in the low pO_2 ambient at 1373 K for 16 hours, Mo(Al$_x$Si$_{1-x}$)$_2$ alloys with x in the range of 0.35–0.65 feature the same surface morphology. As an example, the surface morphology of the oxide scale is shown in Fig. 5a. The surface of the substrate is fully covered with a "grass like" oxide scale. A cross-section of the same sample reveals that the oxide scale is composed of α-Al$_2$O$_3$ exclusively with an Al depletion layer beneath corresponding with Mo$_5$(Al,Si)$_3$; see Fig. 5b.

The microstructure of the alumina scale formed exhibits a distinctive two-layer microstructure; see Fig. 5c. In the outer layer near the surface the grains are equiaxed whereas in the inner layer adjacent to the alloy the grains are columnar. The lateral grain size in the columnar layer is about 0.31 ± 0.10 μm; see Table 2. The elemental mapping in Fig. 5e till i confirms that the oxide scale consists of only Al and O while the adjacent region has a higher Mo to Si ratio than the substrate and contains little Al.

A composition depth profile confirms the presence of the different layers in the Mo(Al$_{0.40}$Si$_{0.60}$)$_2$ alloy after oxidation; see Fig. 5d. The atomic ratio in the oxide scale represents the exclusive formation of

Al$_2$O$_3$. The depletion layer composed of Mo$_5$(Al,Si)$_3$ contains 3.0 at.% Al, which is in agreement with the phase diagram at 1373 K (cf. Fig. 1b) and also with Ref. [18]. No Al gradient was observed within the Mo$_5$(Si,Al)$_3$ layer, suggesting that the diffusion of aluminium in this phase is rapid compared with rate of Al consumption as a result of alumina formation. In the Mo(Si,Al)$_2$ phase adjacent to the Mo$_5$(Al,Si)$_3$ layer also hardly an Al gradient occurs, which implies that also in the Mo(Si,Al)$_2$ phase the diffusion of Al is fast.

In a cross-section of the sample with the highest Al content, i.e., Mo(Al$_{0.65}$Si$_{0.35}$)$_2$, an exclusive α-Al$_2$O$_3$ scale with the layered microstructure and small patches of Mo$_5$(Al,Si)$_3$ at the interface with the oxide scale were observed; see Figs. 6a and 6b. The lateral grain size in the columnar layer is about 0.39 ± 0.20 μm.

The small bright spots having a size of 10–30 nm seen in the STEM image of the alumina scale, see Fig. 6c, are likely composed of Mo$_5$(Al,Si)$_3$ according to XMA. Small pores can be observed in the equiaxed layer of the α-Al$_2$O$_3$ scale; see Figs. 5 and 6.

The α-Al$_2$O$_3$ and Mo$_5$(Al,Si)$_3$ phases were also identified in XRD patterns recorded with Bragg-Brentano geometry; see Fig. 7. Comparing the XRD patterns before and after oxidation (cf. Figs. 3 and 7), shows that transformation of Mo(Al,Si)$_2$ from the orthorhombic (C54) to the hexagonal (C40) crystal lattice structure occurred. This transformation can also be derived from the Mo–Al–Si phase diagram; viz.: the initial Mo(Al,Si)$_2$ phase with an orthorhombic crystal lattice structure at 1773 K lies in the three-phase region of C40, Mo$_5$(Al,Si)$_3$ and Mo$_3$Al$_8$ in the phase diagram at 1373 K when $x > 0.5$; see Figs. 1a and 1b.
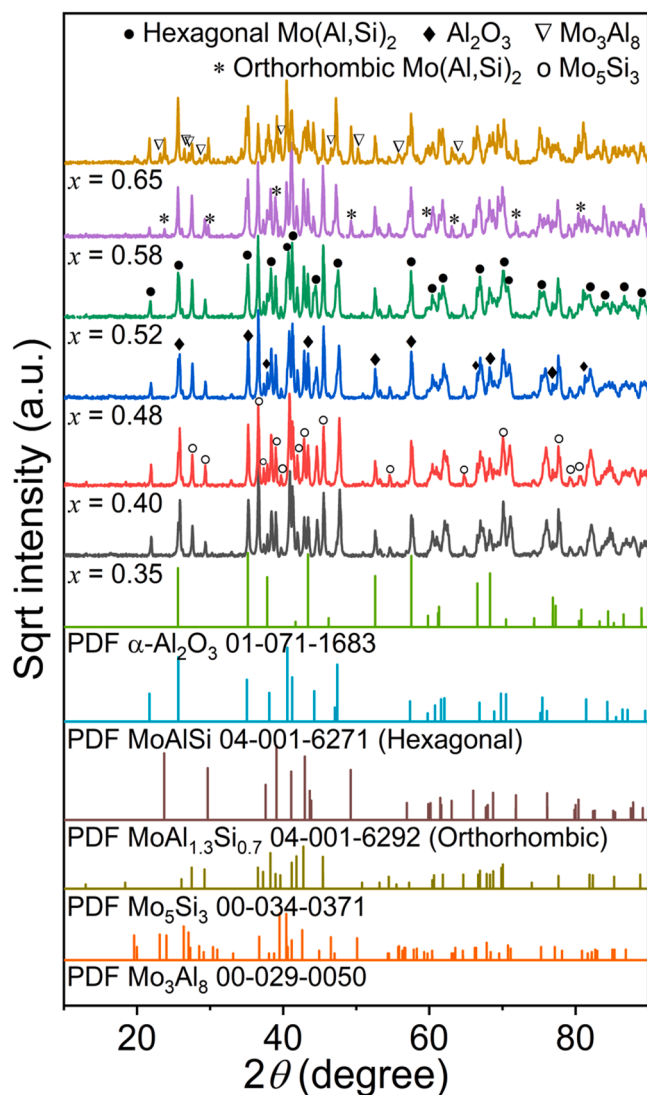
Fig. 7. XRD patterns of Mo(Al$_x$Si$_{1-x}$)$_2$ after 16 hours oxidation in low pO$_2$ (10^{-14} atm.) gaseous ambient at 1373 K recorded with Bragg–Brentano geometry.

3.2.2. Oxidation kinetics

The weight gain per unit surface area of the Mo(Al$_x$Si$_{1-x}$)$_2$ specimens recorded during oxidation at 1373 K in a gaseous ambient with a low pO$_2$ of 10^{-14} atm. is shown in Fig. 8a. Although the weight gain during this oxidation process is rather small, a slight dependence of the oxidation rate on the Al content of Mo(Al$_x$Si$_{1-x}$)$_2$ is observed. The oxidation rate increases with increasing Al content of Mo(Al$_x$Si$_{1-x}$)$_2$.

In an attempt to describe the oxidation process quantitatively, the oxidation kinetics was formulated as a power law with exponent n:

$$\left(\frac{\Delta m}{A}\right)^n = k_m t \tag{1},$$

where Δm is the weight change; A is the surface area of the sample and t the isothermal oxidation time; k_m denotes the oxidation rate constant. The exponent n versus time t can be derived from the mass change data with [31,32]:

$$\frac{1}{n} = \frac{\partial\left(\log\left(\frac{\Delta m}{A}\right)\right)}{\partial(\log(t))} \tag{2}$$

Analysis of the exponent n as a function of oxidation time of the oxide growth curves shows that after an initial transient oxidation period of

about 3 hours (practically independent of the Al content), the oxide growth proceeds with a steady state regime obeying a parabolic growth rate law; see Fig. 8b. The parabolic rate constant increases slightly with the increasing Al content of Mo(Al$_x$Si$_{1-x}$)$_2$; see Fig. 8c.

After the initial transient oxidation period, a layer of Mo$_5$(Al,Si)$_3$ forms beneath the Al$_2$O$_3$ scale and the alloy composition changes along the dashed lines in Fig. 9. The phase constitution and composition can be derived from the tie-lines joining Al-rich region (*C*40) and Al-poor region (D8M); see Fig. 9. For those Mo(Al$_x$Si$_{1-x}$)$_2$ alloys with $x < 0.5$, the alloy composition changes from a single phase position of Mo(Al$_x$Si$_{1-x}$)$_2$ with *C*40 crystal lattice to the two-phase region of Mo(Al$_x$Si$_{1-x}$)$_2$ (*C*40) and Mo$_5$(Al,Si)$_3$ (D8M); while for those Mo(Al$_x$Si$_{1-x}$)$_2$ alloys with $x > 0.5$, the composition changes from Mo(Al$_x$Si$_{1-x}$)$_2$ with *C*54 crystal lattice (formed at 1773 K) into a three-phase region of Mo(Al$_x$Si$_{1-x}$)$_2$ with *C*40 crystal lattice, Mo$_3$Al$_8$ and Mo$_5$(Al,Si)$_3$ after 16 hours oxidation at 1373 K. For the Mo(Al$_x$Si$_{1-x}$)$_2$ alloys with $x < 0.5$, the Al content in the Mo$_5$(Al,Si)$_3$ phase increases with increasing x in Mo(Al$_x$Si$_{1-x}$)$_2$ (see Fig. 8d). And for Mo(Al$_x$Si$_{1-x}$)$_2$ alloys with $x > 0.5$, the fraction of Al rich phase of Mo$_3$Al$_8$ also increases with increasing x in Mo(Al$_x$Si$_{1-x}$)$_2$ after 16 hours oxidation (see Fig. 8d), both of which will accelerate the supply of Al.

To observe the oxide morphology on the surface of the Mo(Al$_x$Si$_{1-x}$)$_2$ alloys during the fast-initial oxidation state, a short term oxidation of Mo(Al$_{0.40}$Si$_{0.60}$)$_2$ was executed at 1373 K in a low pO$_2$ (10^{-14} atm.) gaseous ambient for 1 hour. After this exposure, a discontinuous oxide scale with dimples was observed; see Fig. 10a and b. In these dimples a kind of 'filiform' oxide is seen; see Figs. 10c and 10d. The thickness of the oxide scale in the dimples vary between 200 and 400 nm, while the thickness of the continuous part of the oxide scale is about 1 μm; see Figs. 10e and 10f. The distance between the 'filiform' oxide is comparable with the width of the lateral grain size in the columnar layer. Therefore, the 'filiform' oxide is considered as the new oxide grown on top of the grain boundary of the columnar layer. These so-called 'grain boundary ridges' were also observed in wedge experiments with various types of alumina forming materials [33–36] and was considered as *prima-facie* evidence of oxide formed by outward diffusion of Al along grain boundaries [34].

3.2.3. Oxide scale growth mechanism

It is generally accepted that alumina growth relies on inward and outward diffusion, whereby the relative contributions depend on material, dopants, *etc.* [37,38], whereas the oxidation of chromia formers, for example, the oxide scale is formed primarily by outward diffusion of the metal [34]. There are numerous examples that pointed out that grain-boundary transport of both aluminium and oxygen appears to be the rule in Al$_2$O$_3$ scale-forming Fe-base and Ni-base alloys and the donor or acceptor states of importance must be those associated with the grain boundaries and not with those of the crystal lattice [34,36,39].

The microstructure of the oxide scale on alumina forming alloys and compounds is columnar near the alloy/oxide interface, while equiaxed near the oxide/gas interface [32,34–36,40]. It has been shown by wedge experiments [33–36] that the two-layered microstructure of the grown Al$_2$O$_3$ scale is the result of a so-called "counter-diffusion process" along the grain boundaries, where the inner columnar layer is formed by epitaxial thickening of oxide grains due to inward diffusion of oxygen and the outer equiaxed layer is formed by new oxide growing on top of the grain boundaries of the columnar oxide with repeated coalescence and new oxide creation as a result of the outward diffusion of Al. In the case of Mo(Al$_x$Si$_{1-x}$)$_2$, the same counter-diffusion mechanism is considered to be responsible for the two-layer microstructure of Al$_2$O$_3$ scale formed after oxidation at 1373 K in a low pO$_2$ gaseous ambient; see Figs. 5 and 6.

The growth of an α-Al$_2$O$_3$ layer by selective oxidation of Al in an alloy relies on ionic and electronic transport. In what follows, defect notation of Kröger and Vink [41] is used, wherein the principal lattice species in Al$_2$O$_3$ are represented by O$_O^\times$ and Al$_{Al}^\times$.
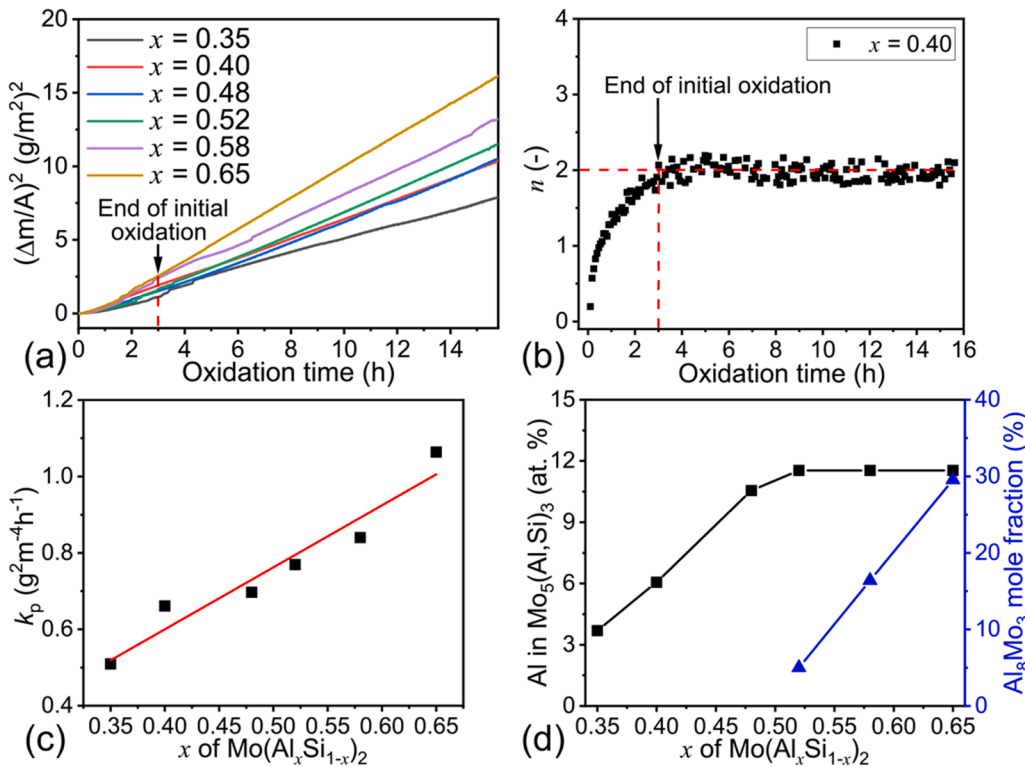
For the scale growth dominated by inward oxygen transport (out-

Fig. 8. (a) Thermogravimetric analysis of the oxidation of $Mo(Al_xSi_{1-x})_2$ in low pO_2 (10^{-14} atm.) gaseous ambient at 1373 K in terms of square weight gain per unit area $(\Delta m/A)^2$ versus oxidation time; (b) Change of the exponent n with time in a power law (cf. Eq. 1); (c) parabolic growth rate constant k_p of the oxidation of $Mo(Al_xSi_{1-x})_2$ (red line: only to guide the eye); (d) Al fraction in the $Mo_5(Al,Si)_3$ (D8M) and the fraction of Al rich phase of Mo_3Al_8 after 16 hours oxidation as determined from the Mo–Al–Si phase diagram at 1373 K.
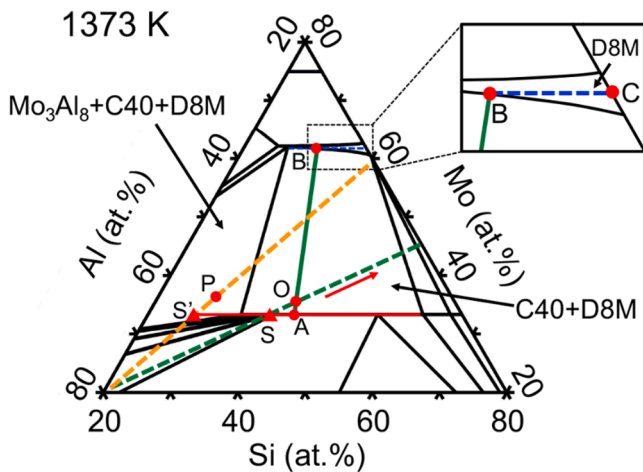

Fig. 9. Partial phase diagram of Mo–Si–Al system at 1373 K, where point S and S′ are the starting compositions of $Mo(Al_{0.40}Si_{0.60})_2$ and $Mo(Al_{0.65}Si_{0.35})_2$ before oxidation, respectively; point O and P are the final compositions of $Mo(Al_{0.40}Si_{0.60})_2$ and $Mo(Al_{0.65}Si_{0.35})_2$ after oxidation; point A and point B are the compositions at Al-rich region and Al-poor region at the equilibrium of point O. C40 pertains to hexagonal $Mo(Al,Si)_2$ and D8M to $Mo_5(Al,Si)_3$.

ward oxygen vacancies diffusion), i.e., the formation of the columnar layer, oxygen vacancies ($V_O^{\cdot\cdot}$) must be annihilated at the scale-gas interface [39] according to:

$$O_2 + 2V_O^{\cdot\cdot} \rightarrow 2O_O^{\times} + 4h^{\cdot} \tag{3}$$

and the growth of new oxide and consumption of substrate metal occurring at the scale-alloy interface follows [39]:

$$2Al_M \rightarrow 3V_O^{\cdot\cdot} + 2Al_{Al}^{\times} + 2V_{Al} + 6e^{'} \tag{4}$$

where Al_M and V_{Al} represent an Al atom and Al vacancy in the Mo–Al–Si alloy. In this case, new oxide develops at the scale-alloy interface and the created Al vacancies must be annihilated at the scale-alloy interface (see Eq. (4)), which is related to the recession of the scale-alloy interface during oxidation.

For the new oxide appearing at the scale-gas interface when outward Al transport (inward diffusion of Al vacancies) dominates, the defect reaction at scale-gas interface can be described as [39]:

$$3O_2 + 12e^{'} \rightarrow 4V_{Al}^{''} + 6O_O^{\times} \tag{5}$$

while consumption of alloy at the scale-metal interface follows [39]:

$$Al_M + V_{Al}^{''} \rightarrow Al_{Al}^{\times} + V_{Al} + 3e^{'} \tag{6}$$

Similarly, vacancy sinks in the substrate must be available as Al vacancies (V_{Al}) are injected into the alloy substrate (Eq. (6)).

The α-Al_2O_3 oxide scale growth rate in the steady state stage (i.e., after the transient oxidation stage, see Fig. 8b) depends on the Al fraction x of the $Mo(Al_xSi_{1-x})_2$ alloy; see Figs. 8a and 8c. This is likely related to the scale/alloy interface concentration which increases with the Al content x of the $Mo(Al_xSi_{1-x})_2$ alloy. The Al activity as the driving force for transport across the scale strongly depends on the Al concentration. An increased activity of Al will result in an enhanced oxidation kinetics due to the accelerated annihilation of cation vacancies [39], cf. Eqs. (4) and (6). The increase of the Al fraction in the $Mo_5(Al,Si)_3$ depletion layer adjacent to the α-Al_2O_3 oxide scale as a function of the Al fraction x of the $Mo(Al_xSi_{1-x})_2$ alloy (see Fig. 8d) points in this direction as well; see also Section 3.2.2.

3.3. High oxygen partial pressure and long-term oxidation

When exposing $Mo(Al_{0.40}Si_{0.60})_2$ bulk alloy in dry synthetic air for another 50 hours after low pO_2 pre-oxidation for 16 hours, a thickened exclusive α-Al_2O_3 scale is formed on the surface; see the XRD result in Fig. 11a and the cross-section in Fig. 11b. After pre-oxidation in the low pO_2 ambient at 1373 K for 16 hours, the oxidation of the Mo
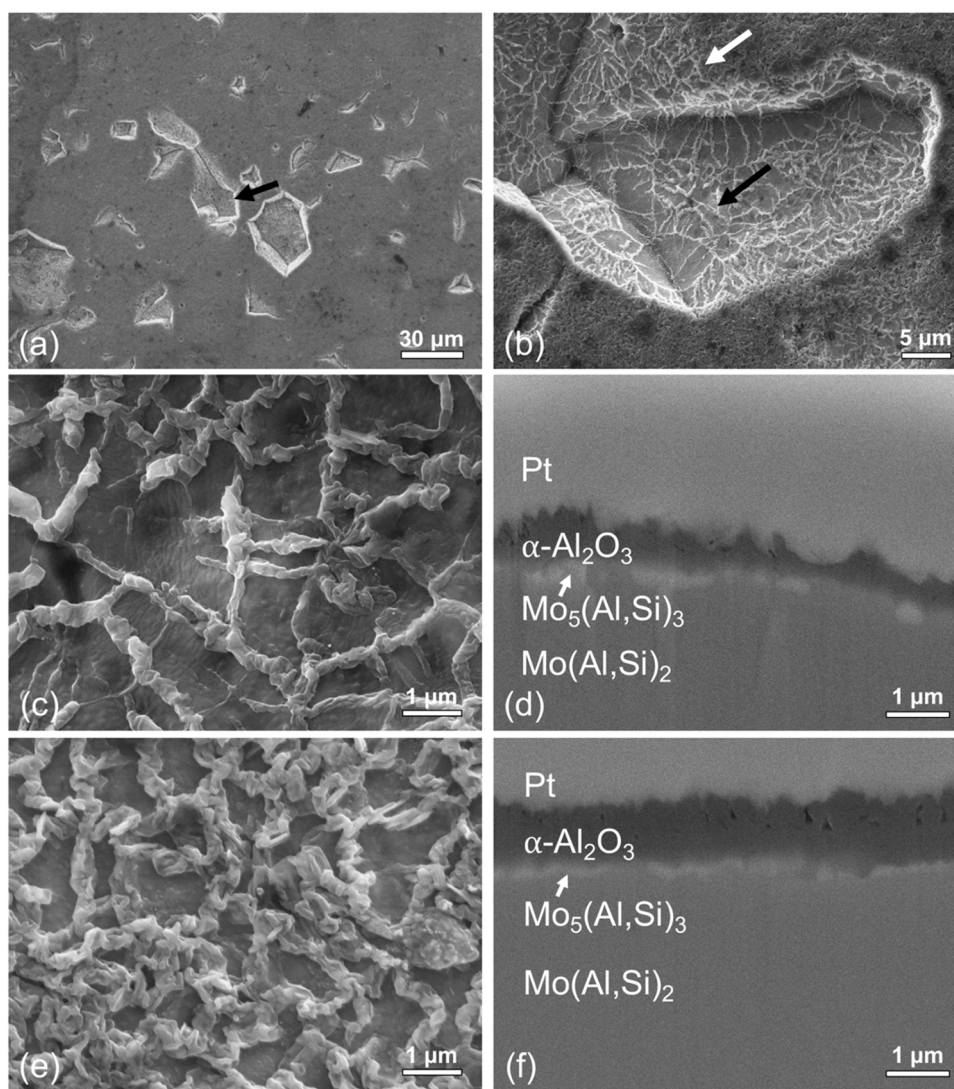
Fig. 10. Morphology of the Mo(Al$_{0.40}$Si$_{0.60}$)$_2$ bulk material after a short term oxidation of 1 hour at 1373 K in low pO$_2$ (10^{-14} atm.) gaseous ambient: (a) SEM image of the surface; (b) detail image of the area indicated with the black arrow in (a); (c) detail image of the dimples indicated with the black arrow in (b); (d) cross-section of the dimples in (c); (e) detail image of the area indicated with the white arrow in (b); (f) cross-section of the area in (e).

(Al$_{0.40}$Si$_{0.60}$)$_2$ in dry synthetic air proceeds similarly as during the pre-oxidation; see Section 3.2.3. The composition depth profile in Figs. 12a and 12b confirms that the oxide layer is composed of α-Al$_2$O$_3$ with adjacent a Mo$_5$(Al,Si)$_3$ depletion layer. The two-layered microstructure of the Al$_2$O$_3$ scale on Mo(Al$_{0.40}$Si$_{0.60}$)$_2$ can still be observed; see Fig. 12c. The equiaxed layer is significantly thickened and densified, while there is only a slight increase in the thickness of the columnar layer; see Table 2. This indicates that the outward diffusion of aluminium ions becomes dominating over the inward diffusion of oxygen during the prolonged oxidation process in the high pO$_2$ gaseous ambient. A similar observation was also made in FeCrAl-based alloys that the Al outward flux contributes significantly to the oxide thickening [34]. After increasing the pO$_2$ from 10^{-14} to 0.21 atm. (dry synthetic air), the weight change shows a continuous steady state regime obeying a parabolic growth rate law; see Fig. 13.

Direct exposure of the Mo(Al$_{0.40}$Si$_{0.60}$)$_2$ alloy to dry synthetic air (pO$_2$ is 0.21 atm.) for 50 hours, i.e., without pre-oxidation in low pO$_2$ ambient, also α-Al$_2$O$_3$ is exclusively formed. XRD analysis (Fig. 11c) and analysis of the cross-section (Fig. 11d and Figs. 14b and 14c) confirm the formation of an exclusive α-Al$_2$O$_3$ scale with adjacent a Mo$_5$(Al,Si)$_3$ depletion layer. Again, the oxide scale exhibits an equiaxed layer on top of a columnar layer; see Fig. 14a. However, this oxide scale formed by

direct exposure to dry synthetic air at 1373 K for 50 hours is thinner and denser than the oxide scale formed after first a pre-oxidation in a low pO$_2$ (10^{-14} atm.) gaseous ambient; cf. Figs. 11d and 14a; see Table 2. The fully dense oxide scale formed, i.e., the equiaxed grained layer without porosity, will effectively inhibit the diffusion process in the oxide scale and thus results in an overall reduction of the oxidation kinetics, which is supported by the lower weight gain and smaller parabolic rate constant (0.25 g^{2}m^{-4}h^{-1} direct exposure vs. 0.70 g^{2}m^{-4}h^{-1} with pre-oxidation); see Fig. 13 and Table 2. Apparently, a closed α-Al$_2$O$_3$ layer is formed at the start of the oxidation preventing the development of volatile Mo-oxide species, because the lower mass gain (see Fig. 13) is not related to material loss but to a slower growth of the oxide scale. Hence, a pre-oxidation of the Mo(Al$_x$Si$_{1-x}$)$_2$ alloys is not required in practice.

After exposure to dry synthetic air for 50 hours, the thickness ratio of the columnar layer to the total oxide scale (0.34) is smaller than that when exposed to low pO$_2$ ambient for 16 hours, 0.34 versus 0.48; see Table 2. The dependence of the growth of the α-Al$_2$O$_3$ scale on the pO$_2$ of the gaseous ambient was demonstrated by a study of the oxygen permeability in non-doped polycrystalline Al$_2$O$_3$ wafers under steep pO$_2$ gradients [42–44]. It was shown that the α-Al$_2$O$_3$ scale exhibits a n-type ionic behaviour at the low pO$_2$ side and a p-type ionic behaviour at high
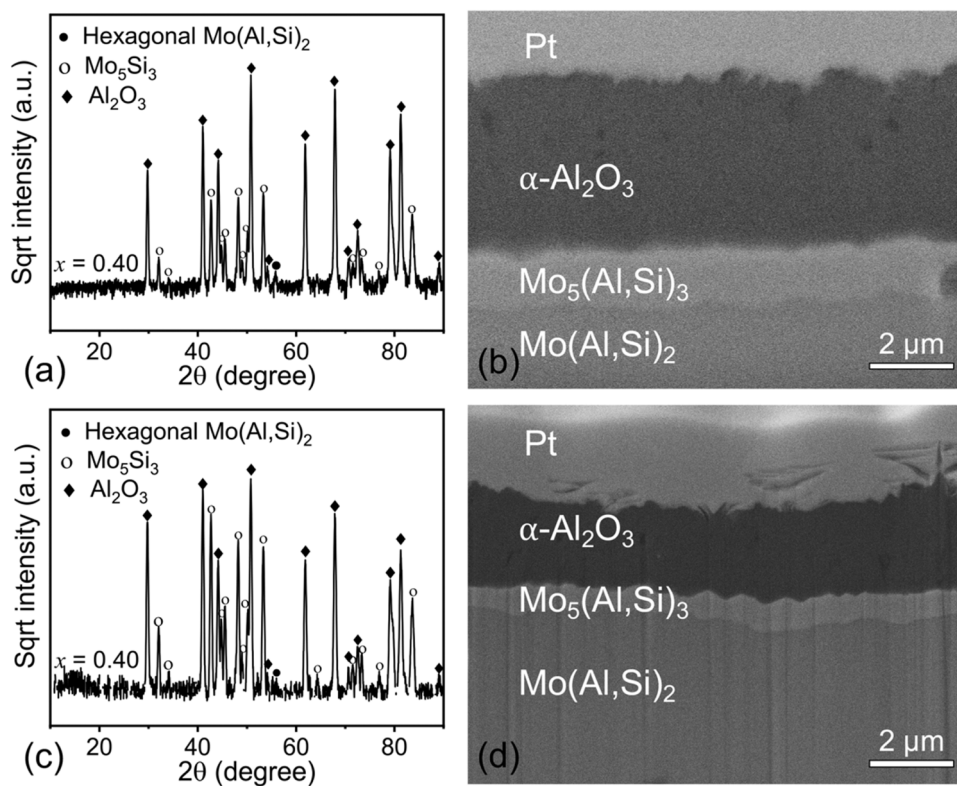
Fig. 11. Mo(Al$_{0.40}$Si$_{0.60}$)$_2$ bulk alloy after oxidation resistance test (first pre-oxidation in low pO$_2$ (10^{-14} atm.) for 16 hours and then oxidation in dry synthetic air for 50 hours at 1373 K): (a) XRD pattern recorded with grazing incidence geometry and (b) cross-section morphology; Mo(Al$_{0.40}$Si$_{0.60}$)$_2$ bulk alloy after direct oxidation in dry synthetic air at 1373 K for 50 hours: (c) XRD pattern recorded with grazing incidence geometry and (d) cross-section morphology.
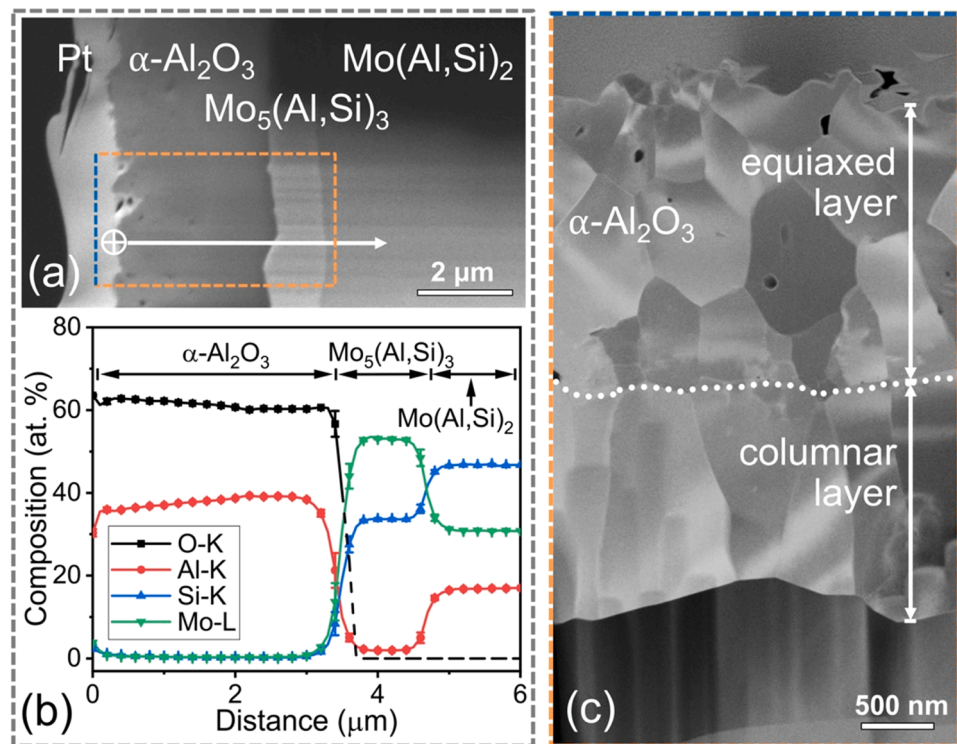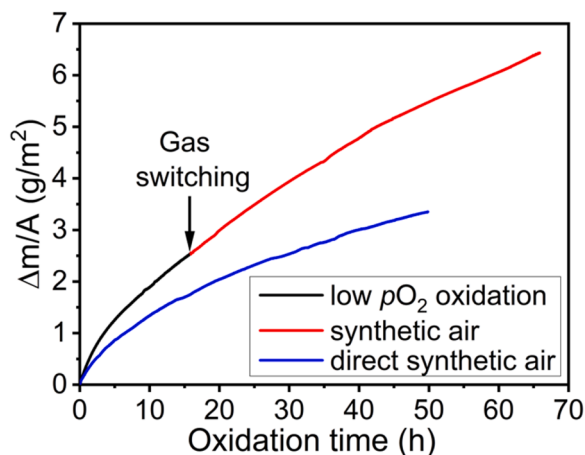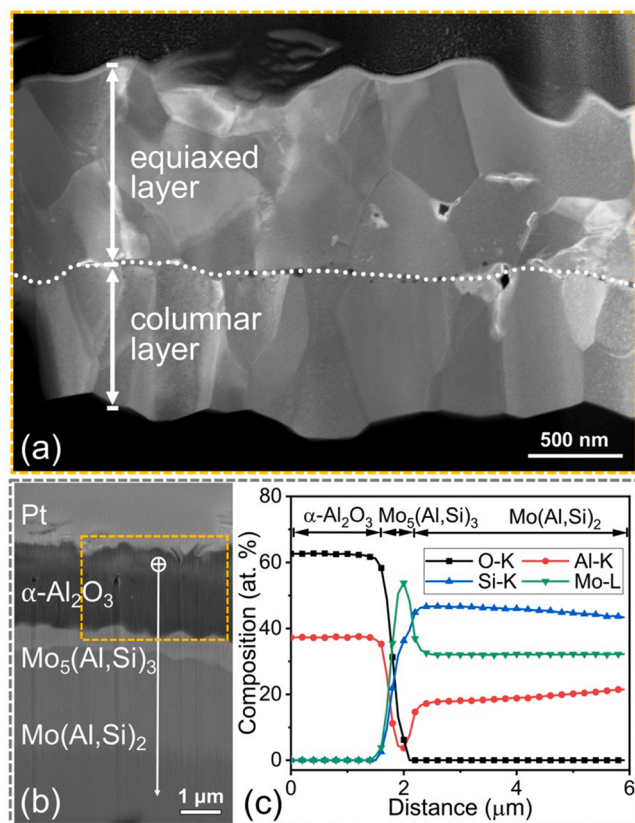

Fig. 12. (a) Position of the composition line scan across the oxide scale, Mo$_5$(Al,Si)$_3$ layer and Mo(Al,Si)$_2$ substrate after 66 hours oxidation (first pre-oxidation in low pO$_2$ of 10^{-14} atm. for 16 hours and then oxidation in dry synthetic air for 50 hours at 1373 K); (b) composition depth profile of Mo(Al$_{0.40}$Si$_{0.60}$)$_2$ bulk alloy after 66 hours oxidation; (c) cross-section (STEM image) of oxide scale on Mo(Al$_{0.40}$Si$_{0.60}$)$_2$ bulk alloy after 66 hours oxidation.

Fig. 13. Thermogravimetric analysis of the oxidation of Mo(Al$_{0.40}$Si$_{0.60}$)$_2$ in terms of weight gain per unit area ($\Delta m/A$) versus oxidation time: first in low pO$_2$ atmosphere (10^{-14} atm.) at 1373 K for 16 hours and then exposed to dry synthetic air for another 50 hours.

Fig. 14. (a) Cross-section (STEM image) of oxide scale on Mo(Al$_{0.40}$Si$_{0.60}$)$_2$ bulk alloy after oxidation in dry synthetic air at 1373 K for 50 hours; (b) position of the composition line scan across the oxide scale, Mo$_5$(Al,Si)$_3$ layer and Mo(Al, Si)$_2$ substrate; (c) composition depth profile of Mo(Al$_{0.40}$Si$_{0.60}$)$_2$ bulk alloy after oxidation in dry synthetic air at 1373 K for 50 hours.

pO$_2$ side, which is correlated with the growth of columnar and equiaxed grains, respectively [42–44]. The n-type behaviour prevails throughout the scale if oxidation occurs at a sufficiently low oxygen partial pressure [42,43]. This explains the thicker columnar layer that was developed when oxidizing Mo(Al$_{0.40}$Si$_{0.60}$)$_2$ in a low pO$_2$ ambient of 10^{-14} atm. as compared with oxidation of this alloy in dry synthetic air (pO$_2$ =

0.21 atm.).

4. Conclusions

Mo(Al$_x$Si$_{1-x}$)$_2$ bulk alloys with Al content *x* varying from 0.35 to 0.65 were prepared by a one-step spark plasma sintering process at 1773 K. The crystal lattice changes from a hexagonal type *C*40 to a orthorhombic type *C*54 with increasing amount of Al substituting Si; i.e, *x* in Mo(Al$_x$Si$_{1-x}$)$_2$.

Upon thermal oxidation of the Mo(Al$_x$Si$_{1-x}$)$_2$ alloys in low oxygen partial pressure atmosphere at 1373 K an oxide scale of exclusively α-Al$_2$O$_3$ was formed with adjacent an Al depleted layer consisting of Mo$_5$(Al,Si)$_3$. A two-layered structure was observed in the α-Al$_2$O$_3$ scale, where the outer layer near the surface consists of grains which are equiaxed whereas in the inner layer adjacent to the alloy the grains are columnar. Phase transformation from orthorhombic (*C*54) to hexagonal (*C*40) crystal lattice occurred due to Al depletion in the Mo(Al,Si)$_2$ as a result of the oxidation process.

The oxidation kinetics obeys an ideal parabolic growth rate law after a short transient oxidation period. The parabolic growth rate constant increased only slightly with the increasing Al content in the Mo(Al$_x$Si$_{1-x}$)$_2$ alloy. A counter-diffusion process of O and Al along grain boundaries of the oxide scale is considered to be responsible for the growth of the α-Al$_2$O$_3$ scale. Dominant inward diffusion of oxygen results in a columnar layer in contact with the alloy, while dominant outward diffusion of Al along grain boundaries of the columnar layer results in formation of the equiaxed layer in contact with the gaseous ambient. During long-term exposure in dry synthetic air after a low oxygen partial pressure oxidation treatment of the Mo(Al$_x$Si$_{1-x}$)$_2$ alloys, outward diffusion of Al contributes significantly to the oxide layer growth.

When the Mo(Al$_x$Si$_{1-x}$)$_2$ alloys are exposed directly to dry synthetic air (high oxygen partial pressure), the α-Al$_2$O$_3$ scale is denser and grows slower as compared to oxidation in a low oxygen partial pressure gaseous ambient. The thickness ratio of the columnar layer to the total oxide scale is smaller than that when exposed to low oxygen partial pressure. Thereby, the formation of dense equiaxed α-Al$_2$O$_3$ layer contributes to excellent oxidation resistance. A low oxygen partial pressure pre-oxidation treatment is not required to mitigate the formation of volatile Mo-oxide species.

CRediT authorship contribution statement

Zhaoying Ding: Investigation, Formal analysis, Visualization, Writing – original draft. **Johannes C. Brouwer:** Experimental validation, Formal analysis, Writing – review & editing. **Cees Kwakernaak:** Experimental validation, Formal analysis, Writing − review & editing. **Marcel J.M. Hermans:** Supervision, Resources, Writing − review & editing. **Vera Popovich:** Supervision, Resources, Writing − review & editing. **Willem J. Quadakkers:** Conceptualization and Writing − review & editing. **Willem G. Sloof:** Conceptualization, Supervision, Resources, Project administration, Writing – review & editing.

Declaration of Competing Interest

The authors declare that they have no known competing financial interests or personal relationships that could have appeared to influence the work reported in this paper.

Data availability

Data will be made available on request.

Acknowledgement

Appendix A

For a gas mixture of CO_2 and CO, the oxygen partial pressure (pO_2) follows from the equilibrium:

$$CO + \frac{1}{2}O_2 \rightarrow CO_2 \tag{A1}$$

with the standard Gibbs free energy expressed as [45]:

$$\Delta G^0 = -282420 + 86.8T \, (J/mol) \tag{A2}$$

where T is the temperature in degree Kelvin. Next, the pO_2 of the gas mixture is related to the ratio of the partial pressures of CO and CO_2, pCO and pCO_2 respectively, according to:

$$pO_2 = \left(\frac{pCO_2}{pCO}\right)^2 \exp\left(\frac{2\Delta G^0}{RT}\right) \tag{A3}$$

References

[1] T. Maruyama, K. Yanagihara, High temperature oxidation and pesting of Mo(Si, Al)$_2$, Mater. Sci. Eng. A (1997) 828–841, https://doi.org/10.1016/S0921-5093(97)00673-4.

[2] A.K. Vasudevan, A comparative overview of molybdenum disilicide composites, Mater. Sci. Eng. A 155 (1992) 1–17, https://doi.org/10.1016/0921-5093(92)90308-N.

[3] T.C. Chou, T.G. Nieh, Mechanism of MoSi$_2$ pest during low temperature oxidation, J. Mater. Res. 8 (1993) 214–226, https://doi.org/10.1017/S0884291400120540.

[4] A.A. Sharif, A. Misra, J.J. Petrovic, T.E. Mitchell, Alloying of MoSi$_2$ for improved mechanical properties, Intermetallics 9 (2001) 869–873, https://doi.org/10.1016/S0966-9795(01)00084-X.

[5] J.J. Petrovic, Mechanical behavior of MoSi$_2$ and MoSi$_2$ composites, Mater. Sci. Eng. A 192/192 (1995) 31–37, https://doi.org/10.1016/0921-5093(94)03246-7.

[6] R. Mitra, R.R. V.V, Effect of minor alloying with Al on oxidation behaviour of MoSi$_2$ at 1200 °C, Mater. Sci. Eng. A 260 (1999) 146–160, https://doi.org/10.1016/S0921-5093(98)00972-1.

[7] J.A. Lemberg, R.O. Ritchie, Mo-Si-B alloys for ultrahigh-temperature structural applications, Adv. Mater. 24 (2012) 3445–3480, https://doi.org/10.1002/adma.201200764.

[8] M. Sundberg, G. Malmqvist, A. Magnusson, T. El-Raghy, Alumina forming high temperature silicides and carbides, Ceram. Int. 30 (2004) 1899–1904, https://doi.org/10.1016/j.ceramint.2003.12.046.

[9] I.M. Wolff, L.E. Iorio, T. Rumpf, S. P.V.T, J.H. Potgieter, Oxidation and corrosion behaviour of Fe–Cr and Fe–Cr–Al alloys with minor alloying additions, Mater. Sci. Eng. A 241 (1998) 264–276, https://doi.org/10.1016/S0921-5093(97)00500-5.

[10] B. Bakhit, J. Palisaitis, J. Thörnberg, J. Rosen, P.O.Å. Persson, L. Hultman, I. Petrov, J.E. Greene, G. Greczynski, Improving the high-temperature oxidation resistance of TiB$_2$ thin films by alloying with Al, Acta Mater. 196 (2020) 677–689, https://doi.org/10.1016/j.actamat.2020.07.025.

[11] C.E. Ramberg, W.L. Worrell, Oxidation kinetics and composite scale formation in the system Mo(Al,Si)$_2$, J. Am. Ceram. Soc. 85 (2002) 444–452, https://doi.org/10.1111/j.1151-2916.2002.tb00109.x.

[12] K. Yanagihara, T. Maruyama, K. Nagata, High temperature oxidation of Mo-Si-X intermetallics (X = Al, Ti, Ta, Zr and Y), Intermetallics 3 (1995) 243–251, https://doi.org/10.1016/0966-9795(95)98935-2.

[13] T. Maruyama, K. Yanagihara, High temperature of oxidation of intermetallic compounds of Mo(Si$_{1-x}$Al$_x$)$_2$, Corros. Sci. 35 (1993) 939–944, https://doi.org/10.1016/0010-938X(93)90312-5.

[14] K. Yanagihara, T. Maruyama, K. Nagata, Effect of third elements on the pesting suppression of Mo-Si-X intermetallics (X = Al, Ta, Ti, Zr and Y), Intermetallics 4 133–139 (1996) 133–139, https://doi.org/10.1016/0966-9795(96)00019-2.

[15] A. Stergiou, P. Tsakiropoulos, A. Brown, The intermediate and high-temperature oxidation behaviour of Mo(Si$_{1-x}$Al$_x$)$_2$ intermetallic alloys, Intermetallics 5 (1997) 69–81, https://doi.org/10.1016/S0966-9795(96)00068-4.

[16] S. Majumdar, I.G. Sharma, S. Raveendra, I. Samajdar, P. Bhargava, *In situ* chemical vapour co-deposition of Al and Si to form diffusion coatings on TZM, Mater. Sci. Eng. A 492 (2008) 211–217, https://doi.org/10.1016/j.msea.2008.03.020.

[17] L. Ingemarsson, K. Hellström, S. Canovic, T. Jonsson, M. Halvarsson, L. G. Johansson, J.E. Svensson, Oxidation behavior of a Mo(Si,Al)$_2$ composite at 900–1600 °C in dry air, J. Mater. Sci. 48 (2012) 1511–1523, https://doi.org/10.1007/s10853-012-6906-0.

[18] L. Ingemarsson, K. Hellström, L.G. Johansson, J.E. Svensson, M. Halvarsson, Oxidation behaviour of a Mo(Si,Al)$_2$ based composite at 1500 °C, Intermetallics 19 (2011) 1319–1329, https://doi.org/10.1016/j.intermet.2011.05.002.

[19] T. Dasgupta, A.M. Umarji, Thermal properties of MoSi$_2$ with minor aluminum substitutions, Intermetallics 15 (2007) 128–132, https://doi.org/10.1016/j.intermet.2006.03.013.

[20] J.B. Wachman, T.G. Scuderi, G.W. Cleek, Linear thermal expansion of aluminum oxide and thorium oxide from 100 to 1100 K, J. Am. Ceram. Soc. 45 (7) (1962) 319–323, https://doi.org/10.1111/j.1151-2916.1962.tb11159.x.

[21] T. Tabaru, K. Shobu, M. Sakamoto, S. Hanada, Effects of substitution of Al for Si on the lattice variations and thermal expansion of Mo(Si,Al)$_2$, Intermetallics 12 (2004) 33–41, https://doi.org/10.1016/j.intermet.2003.07.002.

[22] T. Tabaru, K. Shobu, H. Hirai, S. Hanada, Influences of Al content and secondary phase of Mo$_5$(Si,Al)$_3$ on the oxidation resistance of Al-rich Mo(Si,Al)$_2$-base composites, Intermetallics 11 (2003) 721–733, https://doi.org/10.1016/S0966-9795(03)00072-4.

[23] D.L. Bish, S.A. Howard, Quantitative phase analysis using the Rietveld method, J. Appl. Cryst. 21 (1988) 86–91, https://doi.org/10.1107/S0021889887009415.

[24] J.T. Armstrong, Quantitative elemental analysis of individual microparticles with electron beam instruments, in: Electron Probe Quantitation, Springer, US, Boston, 1991, pp. 261–315.

[25] P.E.A. Turchi, A.L. Landa, Thermodynamic database, lower length scale, part II: thermodynamic assessment of Al-Mo-Si-U (M3MS-12LL0602092), Lawrence Livermore National Laboratory, Tech. Rep. LLNL-TR-603054 (2012) https://www.osti.gov/servlets/purl/1059078.

[26] M.M. Opeka, I.G. Talmy, J.A. Zaykoski, Oxidation-based materials selection for 2000 °C + hypersonic aerosurfaces: Theoretical considerations and historical experienc, J. Mater. Sci. 39 (2004) 5887–5904, https://doi.org/10.1023/B:JMSC.0000041686.21788.77.

[27] H. Li, L. Zhang, Q. Zeng, L. Cheng, Thermodynamic calculation of HfB$_2$ volatility diagram, J. Ph. Equilibria Diffus. 32 (2011) 422–427, https://doi.org/10.1007/s11669-011-9930-x.

[28] R. Inoue, Y. Arai, Y. Kubota, Y. Kogo, K. Goto, Oxidation of ZrB$_2$ and its composites: a review, J. Mater. Sci. 53 (2018) 14885–14906, https://doi.org/10.1007/s10853-018-2601-0.

[29] T.J. Nijdam, L.P.H. Jeurgens, W.G. Sloof, Modelling the thermal oxidation of ternary alloys—compositional changes in the alloy and the development of oxide phases, Acta Mater. 51 (2003) 5295–5307, https://doi.org/10.1016/S1359-6454(03)00381-1.

[30] T.J. Nijdam, L.P.H. Jeurgens, W.G. Sloof, Promoting exclusive α-Al$_2$O$_3$ growth upon high-temperature oxidation of NiCrAl alloys: experiment versus model predictions, Acta Mater. 53 (2005) 1643–1653, https://doi.org/10.1016/j.actamat.2004.12.014.

[31] G.M. Song, V. Schnabel, C. Kwakernaak, S. van der Zwaag, J.M. Schneider, W. G. Sloof, High temperature oxidation behaviour of Ti$_2$AlC ceramic at 1200 °C, Mater. High. Temp. 29 (2014) 205–209, https://doi.org/10.3184/096034012×13348496462140.

[32] D. Naumenko, B. Gleeson, E. Wessel, L. Singheiser, W.J. Quadakkers, Correlation between the microstructure, growth mechanism, and growth kinetics of alumina scales on a FeCrAlY alloy, Metall. Mater. Trans. A 38 (2007) 2974–2983, https://doi.org/10.1007/s11661-007-9342-z.

[33] H.J. Yang, Y.T. Pei, J.T.M.De Hosson, Oxide-scale growth on Cr$_2$AlC ceramic and its consequence for self-healing, Scr. Mater. 69 (2013) 203–206, https://doi.org/10.1016/j.scriptamat.2013.04.013.

[34] J.A. Nychka, D.R. Clarke, Quantification of aluminum outward diffusion during oxidation of FeCrAl alloys, Oxid. Met. 63 (2005) 325–352, https://doi.org/10.1007/s11085-005-4391-4.

[35] V.K. Tolpygo, D.R. Clarke, Microstructural evidence for counter-diffusion of aluminum and oxygen during the growth of alumina scales, Mater. High. Temp. 20 (2014) 261–271, https://doi.org/10.1179/mht.2003.030.

[36] A.H. Heuer, D.B. Hovis, J.L. Smialek, B. Gleeson, Alumina scale formation: a new perspective, J. Am. Ceram. Soc. 94 (2011) s146–s153, https://doi.org/10.1111/j.1551-2916.2011.04573.x.

[37] W.J. Quadakkers, H. Holzbrecher, K.G. Briefs, H. Beske, Differences in growth mechanisms of oxide scales formed on ODS and conventional wrought Alloys, Oxid. Met. 32 (1989) 67–88, https://doi.org/10.1007/BF00665269.

[38] J.L. Smialek, Oxygen diffusivity in alumina scales grown on Al-MAX phases, Corros. Sci. 91 (2015) 281–286, https://doi.org/10.1016/j.corsci.2014.11.030.

[39] A.H. Heuer, T. Nakagawa, M.Z. Azar, P.B. Hovis, J.L. Smialek, B. Gleeson, N.D. M. Hine, H. Guhl, H.S. Lee, P. Tangney, W.M.C. Foulkes, M.W. Finnis, On the growth of Al_2O_3 scales, Acta Mater. 61 (2013) 6670–6683, https://doi.org/10.1016/j.actamat.2013.07.024.

[40] F.A. Golightly, F.H. Stott, G.C. Wood, The relationship between oxide grain morphology and growth mechanisms for Fe-Cr-Al and Fe-Cr-Al-Y alloys, J. Electrochem. Soc. 126 (6) (1979) 1035–1042, https://doi.org/10.1149/1.2129170.

[41] D.J. Young, High temperature oxidation and corrosion of metals, Elsevier, 2008.

[42] M. Wada, T. Matsudaira, S. Kitaoka, Mutual grain-boundary transport of aluminum and oxygen in polycrystalline Al_2O_3 under oxygen potential gradients at high temperatures, J. Ceram. Soc. Jpn. 119 (2011) 832–839, https://doi.org/10.2109/jcersj2.119.832.

[43] T. Matsudaira, M. Wada, T. Saitoh, S. Kitaoka, The effect of lutetium dopant on oxygen permeability of alumina polycrystals under oxygen potential gradients at ultra-high temperatures, Acta Mater. 58 (2010) 1544–1553, https://doi.org/10.1016/j.actamat.2009.10.062.

[44] S. Kitaoka, T. Matsudaira, M. Wada, Mass-transfer mechanism of alumina ceramics under oxygen potential gradients at high temperatures, Mater. Trans. 50 (2009) 1023–1031, https://doi.org/10.2320/matertrans.MC200803.

[45] W. Mao, R.W.A. Hendrikx, W.G. Sloof, Prediction of oxide phases formed upon internal oxidation of advanced high-strength steels, Oxid. Met. 89 (2017) 531–549, https://doi.org/10.1007/s11085-017-9815-4.